A highly stable MOF-engineered FeS_2/C nanocatalyst for heterogeneous electro-Fenton treatment: Validation in wastewater at mild pH

Zhihong Ye,[†] José A. Padilla,[‡] Elena Xuriguera,[‡] José L. Beltran,[§] Francisco Alcaide,[‖] Enric Brillas,[†] and Ignasi Sirés*,[†]

[†] Laboratori d'Electroquímica dels Materials i del Medi Ambient, Departament de Química Física, Facultat de Química, Universitat de Barcelona, Martí i Franquès 1-11, 08028 Barcelona, Spain

[‡] DIOPMA, Departament de Ciència de Materials i Química Física, Facultat de Química, Universitat de Barcelona, Martí i Franquès 1-11, 08028 Barcelona, Spain

[§] Secció de Química Analítica, Departament d'Enginyeria Química i Química Analítica. Universitat de Barcelona, Martí i Franquès 1-11, 08028 Barcelona, Spain

[‖] CIDETEC, Paseo Miramón 196, 20014 Donostia-San Sebastián, Spain

Paper submitted to be published in *Environmental Science and Technology*

*Corresponding author: Tel.: +34 934039240; Fax: +34 934021231.

E-mail address: i.sires@ub.edu (I. Sirés)

ABSTRACT

Herein, the novel application of FeS_2/C nanocomposite as a highly active, stable and recyclable catalyst for heterogeneous electro-Fenton (EF) treatment of organic water pollutants is discussed. The simultaneous carbonization and sulfidation of an iron-based metal organic framework (MOF) yielded well-dispersed pyrite FeS_2 nanoparticles of ~100 nm diameter linked to porous carbon. XPS analysis revealed the presence of doping N atoms. EF treatment with an IrO_2/air-diffusion cell ensured the complete removal of the antidepressant fluoxetine spiked into urban wastewater at near-neutral pH after 60 min at 50 mA with 0.4 g L^{-1} catalyst as optimum dose. The clear enhancement of catalytic activity and stability of the material as compared to natural pyrite was evidenced, as deduced from its characterization before and after use. The final solutions contained < 1.5 mg L^{-1} of dissolved iron and became progressively acidified. Fluorescence excitation−emission spectroscopy with PARAFAC analysis demonstrated the large mineralization of all wastewater components at 6 h, which was accompanied by a substantial decrease of toxicity. A mechanism with $^{\bullet}OH$ as dominant oxidant was proposed: FeS_2 core-shell nanoparticles served as Fe^{2+} shuttles for homogeneous Fenton's reaction and provided active sites for heterogeneous Fenton process, whereas nanoporous carbon allowed minimizing the mass transport limitations.

TABLE OF CONTENTS (TOC) ART

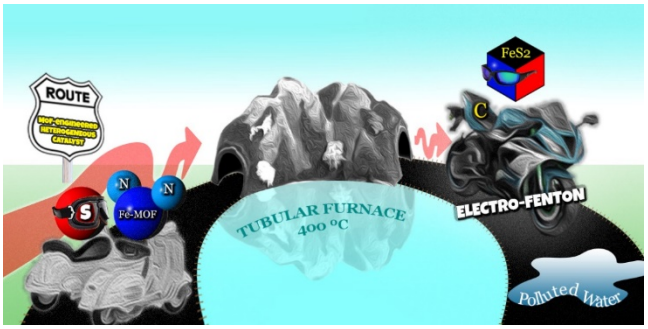

INTRODUCTION

Undoubtedly, Fenton process is currently one of the most attractive technologies to tackle the global water contamination by toxic, recalcitrant, non-biodegradable organic pollutants, owing to its great effectiveness combined with simplicity and low cost.[1] Aiming to overcome some inherent shortcomings,[2] gradual optimization led to the development of electro-Fenton (EF) process, which has become the most successful method among the so-called electrochemical advanced oxidation processes (EAOPs).[3,4] The scientific fundamentals of EF are now quite well understood, but the lack of robustness and reliability of some of the materials involved still hampers its final implementation at industrial scale.[2] On the one hand, much progress has been made on cathode development to enhance the H_2O_2 electrogeneration from the 2-electron O_2 reduction reaction (1).[5] The greatest H_2O_2 accumulation can be achieved using air-diffusion cathodes equipped with a gas chamber,[6-10] although high efficiencies for H_2O_2 production are also feasible with modified three-dimensional carbonaceous cathodes.[11-15] Substantial advances have also been made in the selection of electrocatalytic anodes (M) that promote the simultaneous generation of adsorbed M(•OH) from water oxidation.[16-18]

$$O_{2(g)} + 2H^+ + 2e^- \rightarrow H_2O_2 \quad (1)$$

Conversely, crucial concerns arise when the third cornerstone, i.e., the catalyst, is considered. Conventional EF treatment based on homogeneous catalytic decomposition of H_2O_2 in the presence of soluble Fe^{2+}, according to Fenton's reaction (2) at optimum pH ~ 3.0, is still the sole well-established application.[2]

$$Fe^{2+} + H_2O_2 \rightarrow Fe^{3+} + {}^{\bullet}OH + OH^- \quad (2)$$

Lately, some approaches have been proposed to work at less acidic pH, thus trying to broaden the potential market of EF, which could embrace the treatment of urban

wastewater at near-neutral pH. For example, homogeneous EF is viable at high pH upon use of iron complexed with organic chelators.[19] Nonetheless, heterogeneous catalysts seem a smarter choice, since they can facilitate the post-treatment clean-up and minimize the dissolved iron content that eventually causes sludge production.[20] These catalysts include several types of synthetic iron-loaded structures, such as resins or zeolites,[21,22] as well as zero-valent ion,[2] iron-rich clays[23], layered double hydroxides (LDHs)[24] and minerals like iron oxides[25-27] or pyrite (FeS_2).[26] In particular, mineral pyrite has been confirmed as a very good candidate for Fenton[28,29] or EF[30-32] treatments, since it is an excellent electron donor whose S_2^{2-} conversion to sulfate via reaction (3) and (4) is accompanied by Fe^{2+} and H^+ release. This allows the co-existence of two degradation routes: (i) conventional Fenton's reaction (2), whose occurrence is favored by the gradual acidification, and (ii) heterogeneous Fenton's reaction (5).[30] Although the pyrite-catalyzed EF has shown better performance than other heterogeneous EF treatments, it suffers from excessive iron leaching,[31] which limits the catalyst reusability and requires sludge management.

$$2FeS_2 + 7O_2 + 2H_2O \rightarrow 2Fe^{2+} + 4SO_4^{2-} + 4H^+ \quad (3)$$

$$2FeS_2 + 14Fe^{3+} + 8H_2O \rightarrow 15Fe^{2+} + 2SO_4^{2-} + 16H^+ \quad (4)$$

$$2FeS_2 + 15H_2O_2 \rightarrow 2Fe^{3+} + 14H_2O + 4SO_4^{2-} + 2H^+ \quad (5)$$

Technological development of heterogeneous EF demands the enhancement of catalyst stability. Within this context, synthetic FeS_2[33] and other iron sulfides[34] have revealed an extended life span and greater catalytic activity. In addition, immobilization in carbon-based substrates like graphene oxide may further improve the performance.[35] Lately, metal organic frameworks (MOFs) are being explored as a source for a new generation of highly porous heterogeneous catalysts for water treatment.[36,37] Fe-based MOFs are particularly interesting because of their interconverting Fe(II) and Fe(III)

active sites.[38-40] These structures have been tested in Fenton, either as raw MOFs[41,42] or as precursors of hybrids of Fe-based particles and porous carbon.[43,44] In contrast, the works on the application of MOFs in EF are much more scarce. To our knowledge, MOF-based suspended catalysts have never been employed, and only a small number of MOF-modified cathodes has been reported.[45-47]

This article addresses the synthesis and novel use of a MOF-engineered FeS_2/C nanocomposite, fabricated via simultaneous carbonization and sulfidation of an Fe-MOF precursor that was prepared at room temperature. For the first time, the nanomaterial has been introduced as heterogeneous EF catalyst, focusing on the treatment of fluoxetine spiked into urban wastewater at mild pH as case study because the pollution of freshwater[48,49] and seawater[49,50] by pharmaceuticals has become a serious menace for all living beings. Among them, waterborne antidepressants have proven effects on reproduction and development of vertebrates and invertebrates.[52] Fluoxetine is in the top five psychiatric drugs and, consequently, it has been detected in surface water[52] and wastewater treatment plant effluents.[53] EF could be an interesting alternative to remove fluoxetine from urban wastewater, but it has been validated uniquely for model solutions at pH 3.0.[54] The catalyst characterization before and after use, along with the determination of iron dissolution informed about the stability enhancement. Recyclability and mechanistic conclusions are also provided.

MATERIALS AND METHODS

Chemicals. Fluoxetine hydrochloride was acquired from Sigma-Aldrich. Analytical grade Na_2SO_4, H_2SO_4 solution and NaOH pellets were from Merck. $FeCl_2 \cdot 4H_2O$, 2-methylimidazole and sulfur employed for the synthesis were purchased from Merck and Sigma-Aldrich. Natural pyrite (1.5-4.8 mm grains) was from Alfa Aesar. 1,10-

Phenanthroline monohydrate (Alfa Aesar) and $TiOSO_4$ (Sigma-Aldrich) were used for colorimetric analyses, whereas 5,5-dimethyl-1-pyrroline-N-oxide (DMPO, Sigma-Aldrich) was employed for electron spin resonance (ESR) analysis. Solvents and other reagents were supplied by Panreac and Merck. Unless stated otherwise, the assays were carried out in urban wastewater (Text S1). All CAS numbers and purities are given in Table S1.

Synthesis of the catalyst. The synthetic route followed to obtain the FeS_2/C catalyst, adapted from Pham et al.,[55] is schematized in Figure S1 (Supplementary Information). First, 0.04 mol of 2-methylimidazole was dissolved in 100 mL of ethanol, further adding 0.01 mol of $FeCl_2$•$4H_2O$ to obtain a homogeneous solution that was kept overnight. The slurry obtained upon centrifugation was washed repeatedly and then dried at 80 °C for 12 h. This iron–MOF precursor was carefully mixed with sulfur (with mass ratio 1:2) and transferred to an alumina oxide boat. The mixture was heated up to 400 ºC at 5 ºC min^{-1} in a tube furnace under argon stream, being kept at 400 °C for 2 h. The annealed sample was washed and dried in a vacuum oven at 80 ºC for 24 h. The final FeS_2/C black powder was stored hermetically under N_2 atmosphere.

The performance of the synthesized catalyst was compared with that of commercial pyrite, which was milled and washed with ethanol and nitric acid to obtain the dark shiny powder shown in Figure S1.[30]

Physicochemical characterization of fresh and used catalysts. The X-ray diffraction (XRD) analysis was made using a PANalytical X'Pert PRO MPD Alpha-1 powder diffractometer with Cu $K_{\alpha 1}$ radiation (λ = 1.5406 Å). The morphology was observed by field-emission scanning electron microscopy (FE-SEM) using a JEOL JSM7001F microscope operating at 15 kV and equipped with an Oxford Inca 300 analyzer for energy dispersive spectroscopy (EDS). Samples were also analyzed by high-

137 resolution transmission electron microscopy (HRTEM) using a JEOL JEM-2100 LaB6
138 microscope operating at 200 kV and coupled to the same type of EDS detector for
139 mapping acquisition. In some case, electron energy loss spectroscopy (EELS) spectra and
140 spectrum images were obtained in high angle annular dark-field (HAADF) scanning
141 transmission electron microscopy (STEM) mode employing a FEI Tecnai G2 F20
142 HR(S)TEM operated at 200 kV and coupled to a Gatan Quantum SE 963 imaging filter.
143 EELS spectra were analyzed with Gatan Digital Micrograph software. X-ray
144 photoelectron spectroscopy (XPS) was performed in a PHI 5500 Multitechnique System
145 from Physical Electronics (Text S2). The surface area of particles was determined using
146 the Brunauer–Emmett–Teller (BET) method, using N_2 as the adsorbate gas. The data were
147 obtained using a TriStar 3000 analyzer from Micromeritics. Sample outgass was
148 performed under vacuum for 4 h at 40 ºC. Relative pressures used in the analysis were
149 0.05, 0.10, 0.15, 0.20 and 0.25 (P/P_0). Dynamic light scattering (DLS) was carried out
150 with an LS 13 320 laser diffraction particle size analyzer from Beckman Coulter. The
151 dispersion medium was acetone and samples were sonicated before analysis. Electron
152 spin resonance (ESR) spectra were obtained with a Bruker ESP300E spectrometer at
153 room temperature, using DMPO as the $^{\bullet}OH$ spin trap (Text S3).

154 **Electrochemical degradation and analytical procedures.** The electrolytic trials
155 were performed in an undivided glass cell containing 150 mL of fluoxetine solution
156 thermostated at 30 ºC under vigorous magnetic stirring. The anode (3 cm^2) was either an
157 IrO_2-based plate from NMT Electrodes or a boron-doped diamond (BDD) thin film
158 supplied by NeoCoat. The cathode (3 cm^2) was a commercial carbon cloth coated with
159 carbon-PTFE from BASF, mounted into a purpose-made gas-diffusion holder and fed
160 with compressed air pumped at 1 L min^{-1} for continuous H_2O_2 electrogeneration. The
161 interelectrode gap was about 1.0 cm. Before first use, a polarization in a 0.05 M Na_2SO_4

solution at 100 mA cm^{-2} for 180 min allowed the simultaneous activation of the anode and cathode. The EF treatments were performed after catalyst addition. Galvanostatic electrolyses were performed with an Amel 2053 potentiostat-galvanostat. Catalyst separation or recovery after treatment was made by centrifugation, being able to obtain a clear solution without any trace of catalyst.

The electrical conductance and pH were measured with a Metrohm 644 conductometer and a Crison GLP 22 pH-meter, respectively. Prior all the analyses of samples with iron catalyst, the solids were removed with PTFE syringe filters from Whatman. The H_2O_2 concentration was determined colorimetrically,[8] using a Shimadzu 1800 UV/Vis spectrophotometer set at λ = 408 nm and 25 °C. The total dissolved iron concentration was determined by adding ascorbic acid to the sample, further measuring the light absorption of the colored complex (λ = 510 nm) formed between Fe^{2+} and 1,10-phenantroline. The same spectrophotometer was employed to analyze the active chlorine content by the *N*,*N*-diethyl-*p*-phenylenediamine colorimetric method (λ = 515 nm). TOC was determined on a Shimadzu TOC-VCNS analyzer, which was equipped with a Shimadzu TNM-1 unit for TN analysis. Fluoxetine concentration was determined by reversed-phase high performance liquid chromatography (HPLC), as previously reported,[54] obtaining a narrow peak at retention time of 13.2 min (λ = 227 nm). Duplicate trials were made to correctly assess the mineralization and fluoxetine disappearance, and average values have been plotted along with error bars accounting for 95% confidence level.

Fluorescence excitation−emission matrix (FEEM) spectroscopy was performed using a 1 cm cuvette and an Agilent Cary Eclipse fluorescence spectrophotometer by scanning 351 individual emission wavelengths (250–600 nm) with 5 nm increments of excitation wavelengths between 240 and 460 nm. For each sample, a FEEM was

generated with an intensity value in each coordinate point (Text S4). The interpretation of the FEEM spectra was based on the classification suggested by Chen et al.,[56] who established four component families: aromatic proteins (phenols and indoles), fulvic and UV humic compounds, proteins from microorganisms and visible humic compounds and their hydrolysates. Details on the parallel factor analysis (PARAFAC) modeling can be found in our recent publication.[57] To evaluate the toxicity evolution during fluoxetine treatments, acute bioluminescence inhibition was monitored using *Vibrio fischeri* bacteria (Text S5).

GC-MS analysis was made with an Agilent Technologies system composed of a 6890N gas chromatograph with a 7683B series injector and a 5975 mass spectrometer in electron impact mode at 70 eV (Text S6).

RESULTS AND DISCUSSION

Characterization of the MOF-derived catalyst. The morphology of the as-synthesized catalyst was first evaluated by SEM, a technique that was also employed to evaluate the appearance of the raw iron–MOF precursor. As shown in Figure S2, very small particles became agglomerated to form bigger aggregates of few hundreds of nanometers. On the other hand, the micrographies of the catalyst obtained upon calcination at three lowest magnifications, gathered in Figure S3a, show a uniform distribution of particles with quite homogeneous dimensions. This presumably confirms the validity of the synthesis procedure to obtain a powder containing a large number of regular particles. As depicted in Figure 1a, they had an average size of several hundreds of nanometers. Their particular morphological features can be clearly observed from the largest magnifications, at 33,000× (Figure 1a) and 100,000× (Figure S3a), which reveal that these particles were actually aggregated framboids composed of smaller crystallites

of ca. 100 nm. From the corresponding EDS analysis in Figure S3b, the formation of nanosized Fe–S particles can be plausibly suggested. In addition, the presence of carbon confirms that the sulfidation process allowed the conversion of the organic skeleton of the MOF to carbon. Oxygen appeared in the spectrum as well and, in fact, some dark particles in the SEM contained a higher percentage of this element (~30 wt.% O in regions reach in darker particles versus ~15% in regions with a smaller number). Such particles could then be associated to the formation of a small amount of iron oxides. The particle size distribution determined by DLS is plotted in Figure S3c. The diameter of most of the particles was between 50 and 200 nm, yielding a unimodal distribution with a peak centered at 100 nm. This agrees with the abundance of primary small subparticles found in the SEM images, whose aggregation gave rise to larger secondary nanostructures. Based on this finding, the as-synthesized powder will be properly dispersed by means of ultrasounds prior to its use as catalyst in EF treatments described in next subsections. Worth noting, the size of MOF-derived FeS_2 particles synthesized by sulfidation using other protocols was also around 100 nm.[58] It is expected that nanometric size will have a very positive contribution to the catalytic activity, which will also benefit from a relatively large BET surface area of 25.96 $m^2 g^{-1}$, a value much higher than that reported upon hydrothermal synthesis of FeS_2 (i.e., 1.17 $m^2 g^{-1}$).[33] As expected, the raw iron–MOF precursor had a greater BET surface area of 516.2 $m^2 g^{-1}$, thanks to its inherent 3D porous structure.

The XRD pattern depicted in Figure 1b confirms the good agreement with the structure of pyrite FeS_2, as compared to JCPDS 65-1211 and to natural pyrite used in EF.[30] The main peaks could be associated to (200) plane at 33.1º, (210) at 37.1º, (211) at 40.8º, (220) at 47.4º, and (311) at 56.3º. The high crystallinity of the nanocatalyst can be deduced from the sharp diffraction peaks. Considering the highest one (i.e., at 56.3º), the

crystallite size calculated from Scherrer's equation was 23.4 nm. Therefore, it can be now specified that the nanostructures observed by SEM were pyrite framboids, which were formed as a result of Fe(III) reduction and combination with S during the pyrolysis. The presence of impurities like FeS and iron sulfate was completely discarded, whereas a small amount of Fe_2O_3 (JCPDS 89-0596) was detected, which agrees with the oxygen signal commented above from EDS data. This compound probably appeared via surface oxidation occurring during the synthesis, despite the nitrogen atmosphere, since the final material was stored hermetically before characterization and use. The oxide formation could proceed directly from FeS_2 or, more likely, via $Fe_2(SO_4)_3$ generation and further decomposition.[58]

Morphological characterization with more detailed data on composition was provided by TEM with EDS analysis. The high crystallinity of particles is corroborated from the high-resolution TEM image shown in Figure 1c. A pyrite crystal of 28 nm × 35 nm can be clearly distinguished, surrounded by a blurred area along the perimeter, in good agreement with the crystallite size determined from the XRD pattern. In Figure 1d, several of these structures can be distinguished among the two large aggregates. By analyzing the composition of a few of the individual structures, in close contact with each other, the elements were distributed as highlighted in Figure 1e. The material surrounding the FeS_2 crystal nanoparticles can then be assigned to a carbon shell, eventually giving rise to a core-shell structure. In Figure 1f, another site analyzed by TEM is shown, along with the EDS elemental mapping (note that colors used here do not account for those shown in Figure 1e), but the carbon shell was not so easy to identify. Worth noticing, the signal for oxygen was strong enough, as a result of residual Fe_2O_3, whereas that from nitrogen was very weak. In order to confirm the formation of the core-shell structure, TEM-EELS analysis was carried out. Figure S3d shows the STEM image of an aggregate, along with

261 the EELS spectra recorded from two different regions: region *i*, whose composition agrees
262 with that of a core since it reveals the presence of Fe (major edge at 708 eV (L_3) and a
263 smaller one at 721 eV (L_2)) and S (major edge at 165 eV ($L_{2,3}$)), apart from carbon with
264 a major K-edge at 284 eV; and region *ii*, which clearly matches with a carbon shell.

265 Peaks associated to the carbon shell could not be identified in the XRD pattern due
266 to its amorphous structure. Nonetheless, the Raman spectrum of the FeS_2/C catalyst
267 depicted in Figure S3e evidences the presence of two main bands related to carbon,
268 namely D and G located at 1309 and 1541 cm^{-1}.[59] The smaller peaks at 339 cm^{-1} (E_g), 375
269 cm^{-1} (A_g) and 464 cm_{-1} (T_g) can be attributed to pyrite.[59]

270 The surface composition was further analyzed by XPS. The general spectrum for the
271 as-synthesized FeS_2/C nanocatalyst, depicted in Figure S4, reveals the energy range of
272 the five elements identified above, and the three most important were evaluated in detail.
273 In the high resolution Fe 2p core level XPS spectrum, shown in Figure 2a, both the Fe
274 $2p_{3/2}$ and Fe $2p_{1/2}$ bands consisted of two peaks. The first peak appeared at 707.2 eV,
275 which is very close to the expected value for Fe(II)–S, reported at 707.3 eV[59] and 706.8
276 eV.[29] This confirms the presence of pyrite FeS_2 as the only sulfide on the surface, since
277 there was no peak at 708.9 eV that would correspond to Fe_2S_3.[29] FeS_2 was accompanied
278 by residual Fe_2O_3, displaying a peak at 711.3 eV that matched perfectly with that expected
279 for the Fe(III)–O bond.[59] The two peaks detected in the Fe $2p_{3/2}$ region were confirmed
280 in the Fe $2p_{1/2}$ region. In particular, the Fe(II)–S peak appeared at 720.2 eV, which is
281 closed either to 719.8 eV[60] or 720.0 eV.[59] In the high resolution S 2p of Figure 2b, the
282 peak for S $2p_{3/2}$ appeared at 162.9 eV, in good agreement with that reported for S_2^{2-} at
283 162.7 eV[29] and 162.2 eV.[60] The presence of this sulfide was confirmed in the S $2p_{1/2}$
284 region, since the experimental peak at 163.9 eV matched very well with the expected
285 signal at 164.0 eV.[59] No peaks were found within the region from 166 to 168 eV, which

allows discarding the presence of stable SO_4^{2-} and SO_3^{2-}. Figure 2c shows the peaks that appeared after deconvolution of the N 1s band, which resulted from the presence of N atoms in the MOF. Upon sulfidation at high temperature, the iron–MOF collapsed with the formation of water vapor, CO_x and *N*-containing gases. However, some N remained as a dopant in the solid carbon, forming C–N bonds. In particular, two types of positions were occupied by N: (i) pyridinic, at 399.3 eV, which is close to that reported at 398.6 eV;[61] and (ii) graphitic, at 400. 7 eV, also close to 401.1 eV previously reported.[61] N-doping of carbon is another interesting feature of the synthesized FeS_2/C nanocatalyst, since it has been reported to enhance the catalytic activity.[14] Finally, the spectrum of carbon presented a sole peak, at 284.6 eV (not shown).[58]

Removal of fluoxetine from urban wastewater by heterogeneous EF process. In Figure 3a, fluoxetine removal during the treatment of solutions containing 0.049 mM drug (10 mg C L^{-1}) spiked into urban wastewater by various electrochemical processes using an IrO_2/air-diffusion cell at 50 mA is compared. As expected, a small removal of 41% was attained after 60 min via electrochemical oxidation with electrogenerated H_2O_2 (EO-H_2O_2) at initial pH 3.0, since H_2O_2 produced from reaction (1) and $IrO_2(^{\bullet}OH)$ generated on the anode surface have a low oxidation ability.[3,4,6] In fact, the drug disappearance was mainly caused by active chlorine (i.e., residual steady state concentration of 4-6 mg L^{-1}) produced via Cl^- oxidation at IrO_2. Homogeneous EF at pH 3.0 is known to be much more effective thanks to the formation of $^{\bullet}OH$ from Fenton's reaction (2), but only a slight degradation enhancement was achieved, ending in 47% removal. This can be explained by the excessively low Fe^{2+} catalyst concentration, i.e., 5 mg L^{-1} (within the range of the amount of dissolved iron during heterogeneous EF, as explained below). It yielded the quickest drug disappearance until 15 min of electrolysis, whereupon the removal rate sharply decreased. The air-diffusion cathode exhibits a poor ability to regenerate Fe^{2+} via

electrochemical Fe^{3+} reduction and hence,[2,3] the catalyst content from 15 min was rather low and accumulated in its less active form. In IrO_2/air-diffusion cells, the optimum Fe^{2+} catalyst concentration is in the range 27-55 mg L^{-1}.[8-10] Heterogeneous EF catalyzed with 0.5 g L^{-1} natural pyrite at initial pH 6.0 showed the lowest performance, attaining a fluoxetine concentration decay as low as 19%. Some authors have reported a fast pollutant removal by pyrite-EF,[30-32] but in those trials current was supplied once the spontaneous acidification and iron release had occurred. Conversely, poor performance of commercial pyrite at near-neutral pH was reported upon immediate Fenton treatment of alachlor.[33] On the other hand, the apparently surprising slow degradation as compared to EO-H_2O_2 can be justified by the substantial destruction of active chlorine on the catalyst surface. Figure 3a shows that the FeS_2/C-catalyzed heterogeneous EF process at initial pH 6.0 clearly outperformed all the other treatments, reaching 91% drug removal. This outstanding result can be accounted for by the cooperation between homogeneous and heterogeneous Fenton's reaction as main mechanisms. The former was supported by the detection of 1.40 mg L^{-1} of dissolved iron ion and the solution acidification ending in pH 3.0, as show in Figure 3b, eventually yielding $^{\bullet}OH$ via reaction (2). Considering the low dissolved iron concentration, the second mechanism is expected to have a crucial role. In addition, the presence of Fe–S bonds maximized the contribution of heterogeneous catalysis,[34] which involved the H_2O_2 decomposition, pre-eminently at Fe(II) sites.[29] Several factors contribute to the superiority of the novel heterogeneous EF process over pyrite-EF. As can be seen in Figure 3b, only 0.28 mg L^{-1} iron were dissolved at 60 min and pH was not so acidic, which limited the participation of reaction (2). Regarding the surface-related Fenton's reaction: (i) the FeS_2/C catalyst was nanosized, thus offering a much larger area; (ii) molecular O_2 activation could be induced by a higher content of surface-bound Fe(II) on FeS_2, promoting the generation of superoxide radical ($O_2^{\bullet-}$);[33]

and (iii) the presence of carbon enhanced both, the mass transport due to its porosity, and the catalytic activity, as also found for Fe_3O_4/C catalyst during octane degradation.[62] The reactivity was also favored by doping with N.

It is very remarkable that iron release with the new catalyst was much lower than that reported for pyrite-EF process with pre-dissolution (1.5 vs > 8 mg L^{-1}).[30,31] The great stability of FeS_2/C was confirmed in all subsequent trials. Figure S5a informs about the need of preliminary stripping in order to remove CO_3^{2-} and HCO_3^- from the urban wastewater. Otherwise, fluoxetine removal was only 25%, owing to: (i) catalyst passivation by calcium and magnesium carbonates and phosphates that impeded acidification (Figure S5b) and iron dissolution (Figure S5c) according to reactions (3)-(5), and (ii) the well-known role of CO_3^{2-} and HCO_3^- as radical scavengers.[3] Note that stirring of the catalyst suspension before current supply seems to cause adsorption to some extent. This can be better interpreted from Figure S6, which shows the trend of fluoxetine concentration when the treatment with FeS_2/C of Figure 3 and S3 was made without current supply. The particles had an adsorption capacity around 30% during the first minutes (Figure S6a), mainly attributed to the carbon porosity, which occurred in concomitance with a poor pH decrease and iron release (Figure S6b and S6c). However, the interactions were weak and fluoxetine became completely desorbed again. This confirms that drug removal during EF treatment was caused by oxidative Fenton-based reactions. Another relevant conclusion is the preponderance of reaction (5) over (3) and (4) as the cause for Fe^{2+} and H^+ release.

Aiming to estimate the percentage of contribution of heterogeneous catalysis to the global degradation reached by EF with FeS_2/C (91%, Figure 3a), an analogous experiment was made but replacing the wastewater by a phosphate buffer solution (Figure S7a), which kept the pH constant (~ 6.0, Figure S7b). At such high pH, the dissolved iron was

almost negligible (< 0.25 mg L^{-1}, Figure S7c) and hence, the contribution of homogeneous Fenton's reaction to the final 46% drug removal could be presumed as insignificant. Since in EO-H_2O_2 in phosphate buffer the degradation at 60 min was 20% (Figure S7a), it could be inferred that the FeS_2/C catalyst is able to yield 26% fluoxetine degradation via pure heterogeneous catalysis. Now, going back to Figure 3a, as a first approach one could conclude that the 91% drug removal was caused by a combined mechanism involving heterogeneous Fenton (~26%, as just calculated form Figure S7a) and EO-H_2O_2 (~41%, Figure 3a), but being also remarkable the role of homogeneous Fenton (~24%). From Figure 3a, a minor contribution of the latter mechanism was expected, but in practice the gradual iron leaching stimulated upon natural acidification (Figure 3a) is actually demonstrated to exert a positive impact on decontamination. An additional EO-H_2O_2 experiment in 0.05 M Na_2SO_4 (Figure 3a, 22% removal) allowed us to refine the calculation: ~50% of removal was caused by FeS_2/C-induced Fenton-based reactions, with heterogeneous Fenton having a leading role with support from homogeneous Fenton (despite the fact that, in wastewater at pH 6.0, homogeneous EF behaved similarly to EO-H_2O_2, which is attributed to the enhanced $^{\bullet}OH$ destruction upon single Fe^{2+} addition and the limited Fe^{2+} regeneration), 22% was purely due to EO-H_2O_2 and 19% to oxidation by active chlorine. Note that fluoxetine removal from wastewater at pH 7.0 has been revealed very successful with the latter oxidant.[63] Anyway, the participation of other potential oxidants like chlorine radicals is not discarded either. In summary, these findings confirm the complex mechanisms arising from the use of the FeS_2 nanocatalyst.

The effect of pH, catalyst dosage, applied current and anode on the normalized fluoxetine concentration decay upon heterogeneous EF treatment with FeS_2/C is shown in Figure 4. As can be observed in Figure 4a, the removal rate was enhanced at more acidic initial pH, in agreement with the gradually lower final pH and slightly higher

dissolved iron concentration (Figure S8), which promoted the occurrence of Fenton's reaction (2). Overall disappearance was reached at pH 4.0, although it can be concluded that the treatment was valid within all the pH range (4.0-8.0). As expected, the use of a larger amount of catalyst progressively from 0.1 to 0.4 g L^{-1} allowed a faster removal (Figure 4b), which was due both to the greater contribution of heterogeneous catalysis and homogeneous Fenton's reaction thanks to more dissolved iron (see Figure S9). However, further increase to 0.5 g L^{-1} FeS_2/C did not improve the performance, probably because of the parasitic reaction between $^{\bullet}OH$ and the excess of Fe(III) or Fe(II). Figure 4c evidences the positive contribution of current increase, being more significant from 15 to 30 mA, which resulted from a gradually greater iron release (Figure S10a) and H_2O_2 electrogeneration (Figure S10b). The latter species had a prevailing role due to its higher concentration, which affected the availability of $^{\bullet}OH$ because of its parasitic consumption. Finally, the replacement of the anode by RuO_2 or BDD had an important impact on the degradation rate, attaining the total removal at 60 and 50 min, respectively (Figure 4d). This was feasible by the greater active chlorine concentration produced in the former case, and the more active $^{\bullet}OH$ in the latter one because of its physisorbed nature.[3,4] Evidences to support these explanations have been reported elsewhere.[6,64]

In all the trials, the preponderant role of $^{\bullet}OH$ as main oxidant species has been assumed. This was further confirmed by performing the EF treatment as in Figure 3a but in the presence of a radical scavenger, *p*-benzoquinone for $O_2^{\bullet-}$ and *tert*-butanol for $^{\bullet}OH$.[3,4,28] From Figure S11a it is clear that, although some authors highlighted the former radical produced by pyrite,[28] it played a minor role in the FeS_2/C-catalyzed EF. This agrees perfectly with Liu et al.,[33] who reported a 71-fold enhancement of the production rate constant of $^{\bullet}OH$ using non MOF-derived FeS_2 instead of pyrite. The presence of $^{\bullet}OH$ was corroborated via ESR analysis (Figure S11b).

411 Figure S12a shows the recyclability of the catalyst. A small but progressive
412 performance decay was observed and, after 5 cycles, fluoxetine removal at 60 min was
413 61% as maximum. However, proper cleaning with organic solvent (CH_2Cl_2) and water
414 allowed its complete regeneration. Note that the solvent can be reused several times for
415 successive cleaning of exhaust catalyst. Figure S12b evidences a lower iron dissolution
416 from cycle 1 to 5, further recovered upon surface conditioning. The adsorption of natural
417 organic matter (NOM) and/or precipitates could probably explain the performance decay.
418 To ascertain this, the as-synthesized catalyst was suspended in urban wastewater for 5
419 min, then rinsed with Milli-Q water and dried. Finally, the hypothesized organics
420 adsorbed on the catalyst surface were redissolved via extraction with CH_2Cl_2. Five
421 organic components, typically found in urban wastewater, were identified (Table S2),
422 which confirms the feasibility of poisoning of catalyst by NOM. Note that most of
423 published works report a higher recyclability, around 80-90%, but in model solutions
424 without NOM. The catalyst was characterized after the 5^{th} cycle in order to better
425 elucidate the loss of performance. The SEM images in Figure S13a reveal a certain
426 agglomeration of particles, forming larger framboids but still maintaining the nanometric
427 subparticles. The EDS analysis (Figure S13b) evidences the presence of P, which
428 confirms the precipitation of insoluble phosphates on the catalyst surface. Worth noting,
429 the crystalline pyrite structure was stable along the treatment (Figure S13c), without any
430 new alteration. Similarly, the high resolution Fe 2p core level XPS spectrum shown in
431 Figure 13d confirms the predominance of FeS_2 (peaks at 706.2 and 719.1 eV) over Fe_2O_3
432 (712.5 and 725.5 eV) on the catalyst surface. It is worth highlighting that, upon use in EF
433 process, a third peak appeared in the Fe $2p_{3/2}$ and Fe $2p_{1/2}$ bands at 709.6 and 723.6 eV,
434 respectively. This can be plausibly attributed to the formation of FeO, whose bands are

typically found at 709.7 and 722.7 eV,[65] mainly as a result of the partial reduction of Fe_2O_3 to FeO from heterogeneous Fenton-like reaction with H_2O_2.

Mineralization and proposed mechanism. Longer trials were performed to assess the mineralization ability of the heterogeneous EF treatment, using the optimum FeS_2/C content shown in Figure 4b (i.e., 0.4 g L^{-1}). A BDD anode and a current of 100 mA were employed, looking for a more powerful system thanks to the production of physisorbed $^{\bullet}OH$. It was a right choice since, as can be seen in Figure S14, an impressive 90% TOC removal was achieved at 6 h. This outperforms even the conventional EF process at pH 3.0, which typically yields TOC removals of 60% as maximal due to the accumulation of very refractory Fe(III) complexes with aliphatic organics.[2] In the present system, a very small amount of such complexes can be accumulated because the dissolved iron concentration was always low. Hence, the previously reported fluoxetine aromatic intermediates could be gradually degraded.[54] As illustrated, the toxicity increased during the first 120 min, as expected from the formation of chlorinated intermediates and oxychlorine anions.[54] Thereafter, the solution became much less toxic, reaching an EC_{50} of 110 mg L^{-1} that was twice the initial (i.e., toxicity was halved).

FEEM analysis was made during the same trial to obtain more specific information on the nature and time course of dissolved organic matter. In Figure 5a, the almost complete disappearance of the fluorescence signals after 120-180 min (samples 4-5) can be observed. As revealed in Figure S15a, five kinds of components (C1-C5) were identified upon PARAFAC analysis of the spectra of the seven samples. The plots on the left correspond to the FEEM spectra of components, whereas on the right the emission and excitation signals for each one can be seen. Component C1, exhibiting the maxima at 260/296 nm (excitation/emission), was related to fluoxetine,[66] which was practically absent in urban wastewater (sample 1). C2 exhibited at 280/330 nm, was related to soluble

460 microbial by-products. C3 comprised two pairs of peaks, at 280/485 and 400/485 nm, in
461 agreement with those of humic-like substances. C4 was also characterized by two pairs
462 of peaks, at 320/390 and 290/390 nm, associated to fulvic acids. Finally, C5 exhibited
463 peaks at 250/440 and 345/440 nm and it was explained by the presence of humic-like
464 substances.[57] Components C2-C5 accounted for the NOM mentioned in previous
465 subsection. According to Figure S15b, five components was a good choice for PARAFAC
466 model, since the standard deviation did not decrease significantly when a larger number
467 of components was considered. The distribution of components C1-C5 in samples 1-7 of
468 Figure 5a is depicted in Figure 5b, where it is confirmed that at 120 min (sample 4) there
469 was no more fluoxetine and in sample 5 (180 min of electrolysis) all the fluorescent
470 organic compounds had disappeared. Therefore, the residual TOC in Figure S14
471 corresponded to aliphatic products.

472 Taking into account the main homogeneous and heterogeneous reactions and species
473 mentioned throughout the manuscript, a thorough mechanism is proposed in Figure 6 for
474 the FeS_2/C-catalyzed EF treatment of fluoxetine, as model organic pollutant, at mild pH.
475 In conclusion, the pyrite-like nanocomposite made of a nanosized FeS_2 core embedded in
476 a carbon shell has been confirmed as an outstanding candidate for heterogeneous EF
477 treatment, showing a high activity and large reusability, thus minimizing the capital
478 expenses and avoiding the need of post-treatment sludge management.

479 **ASSOCIATED CONTENT**

480 Supporting Information (SI) contains Text S1-S5, and Figures S1-S13. This
481 information is available free of charge on the ACS Publications website.

482 **ACKNOWLEDGMENT**

The authors gratefully acknowledge financial support from project CTQ2016-78616-R (AEI/FEDER, EU). The PhD scholarship awarded to Z. Ye (State Scholarship Fund, CSC, China) is also acknowledged.

REFERENCES

(1) Zhang, M.; Dong, H.; Zhao, L.; Wang, D.; Meng, D. A review on Fenton process for organic wastewater treatment based on optimization perspective. *Sci. Total Environ.* **2019**, *670*, 110-121; DOI 10.1016/j.scitotenv.2019.03.180.

(2) Zhou, M.; Oturan, M. A.; Sirés, I. Electro-Fenton Process: New Trends and Scale-Up, *Springer Nature*, Singapore, **2018**.

(3) Sirés, I.; Brillas, E.; Oturan, M. A.; Rodrigo, M. A.; Panizza, M. Electrochemical advanced oxidation processes: today and tomorrow. a review. *Environ. Sci. Pollut. Res.* **2014**, *21*, 8336-8367; DOI 10.1007/s11356-014-2783-1.

(4) Martínez-Huitle, C. A.; Rodrigo, M. A.; Sirés, I.; Scialdone, O. Single and coupled electrochemical processes and reactors for the abatement of organic water pollutants: a critical review. *Chem. Rev.* **2015**, *115* (24), 13362-13407; DOI 10.1007/s11356-014-2783-1.

(5) Zhou, W.; Meng, X.; Gao, J.; Alshawabkeh, A. N. Hydrogen peroxide generation from O_2 electroreduction for environmental remediation: A state-of-the-art review. *Chemosphere* **2019**, *225*, 588-607; DOI 10.1016/j.chemosphere.2019.03.042.

(6) Galia, A.; Lanzalaco, S.; Sabatino, M. A.; Dispenza, C.; Scialdone, O.; Sirés, I. Crosslinking of poly(vinylpyrrolidone) activated by electrogenerated hydroxyl radicals: a first step towards a simple and cheap synthetic route of nanogel vectors. *Electrochem. Commun*. **2016**, *62*, 64-68; DOI 10.1016/j.elecom.2015.12.005.

(7) Roth, H.; Gendel, Y.; Buzatu P.; David, O.; Wessling, M. Tubular carbon nanotube-based gas diffusion electrode removes persistent organic pollutants by a cyclic adsorption – Electro-Fenton process. *J. Hazard. Mater.* **2016**, *307*, 1-6; DOI 10.1016/j.jhazmat.2015.12.066.

(8) Lanzalaco, S.; Sirés, I.; Sabatino, M. A.; Dispenza, C.; Scialdone, O.; Galia, A. Synthesis of polymer nanogels by electro-Fenton process: investigation of the effect of main operation parameters. *Electrochim. Acta*. **2017**, *246*, 812-822; DOI 10.1016/j.electacta.2017.06.097.

(9) Salmerón, I.; Plakas, K. V.; Sirés, I.; Oller, I.; Maldonado, M. I.; Karabelas, A. J.; Malato, S. Optimization of electrocatalytic H_2O_2 production at pilot plant scale for solar-assisted water treatment. *Appl. Catal. B: Environ.* **2019**, *242*, 327-336; DOI 10.1016/j.apcatb.2018.09.045.

(10) Ye, Z.; Guelfi, D. R. V.; Álvarez, G.; Alcaide, F.; Brillas, E.; Sirés, I. Enhanced electrocatalytic production of H_2O_2 at Co-based air-diffusion cathodes for the photoelectro-Fenton treatment of bronopol. *Appl. Catal. B: Environ.* **2019**, *247*, 191-199; DOI 10.1016/j.apcatb.2019.01.029.

(11) Le, T. X. H.; Bechelany, M.; Cretin, M. Carbon felt based-electrodes for energy and environmental applications: A review. *Carbon* **2017**, *122*, 564-591; DOI 10.1016/j.carbon.2017.06.078.

(12) Pérez, T.; Coria, G.; Sirés, I.; Nava, J. L.; Uribe, A. R.; Electrosynthesis of hydrogen peroxide in a filter-press flow cell using graphite felt as air-diffusion cathode. *J. Electroanal. Chem.* **2018**, *812*, 54-58; DOI 10.1016/j.jelechem.2018.01.054.

(13) Su, P.; Zhou, M.; Lu, X.; Yang, W.; Ren, G.; Cai, J. Electrochemical catalytic mechanism of N-doped graphene for enhanced H_2O_2 yield and in-situ degradation of

organic pollutant. *Appl. Catal. B: Environ.* **2019**, *245*, 583-595; DOI 10.1016/j.apcatb.2018.12.075.

(14) Yang, W.; Zhou, M.; Oturan, N.; Li, Y.; Su, P.; Oturan, M. A.; Enhanced activation of hydrogen peroxide using nitrogen doped graphene for effective removal of herbicide 2,4-D from water by iron-free electrochemical advanced oxidation. *Electrochim. Acta* **2019**, *297*, 582-592; DOI 10.1016/j.electacta.2018.11.196.

(15) Yang, W.; Zhou, M.; Oturan, N.; Li, Y.; Oturan, M. A. Electrocatalytic destruction of pharmaceutical imatinib by electro-Fenton process with graphene-based cathode. *Electrochim. Acta* **2019**, *305*, 285-294; DOI 10.1016/j.electacta.2019.03.067.

(16) Sirés, I.; Low, C. T. J.; Ponce-de-León, C.; Walsh, F. C. The deposition of nanostructured β-PbO_2 coatings from aqueous methanesulfonic acid for the electrochemical oxidation of organic pollutants. *Electrochem. Commun.* **2010**, *12*, 70-74; DOI 10.1016/j.elecom.2009.10.038.

(17) Oturan, N.; Ganiyu, S. O.; Raffy, S.; Oturan, M. A. Sub-stoichiometric titanium oxide as a new anode material for electro-Fenton process: Application to electrocatalytic destruction of antibiotic amoxicillin. *Appl. Catal. B: Environ.* **2017**, *217*, 214-223; DOI 10.1016/j.apcatb.2017.05.062.

(18) Olvera-Rodríguez, I.; Hernández, R.; Medel, A.; Guzmán, C.; Escobar-Alarcón, L.; Brillas, E.; Sirés, I.; Esquivel, K. TiO_2/Au/TiO_2 multilayer thin-film photoanodes synthesized by pulsed laser deposition for photoelectrochemical degradation of organic pollutants. *Sep. Purif. Technol.* **2019**, *224*, 189-198; DOI 10.1016/j.seppur.2019.05.020.

(19) Ye, Z.; Brillas, E.; Centellas, F.; Cabot, P. L.; Sirés, I. Electro-Fenton process at mild pH using Fe(III)-EDDS as soluble catalyst and carbon felt as cathode. *Appl. Catal. B: Environ.* **2019**, *257*, 117907; DOI 10.1016/j.apcatb.2019.117907.

(20) Ganiyu, S. O.; Zhou, M.; Martínez-Huitle, C. A. Heterogeneous electro-Fenton and photoelectro-Fenton processes: a critical review of fundamental principles and application for water/wastewater treatment. *Appl. Catal. B: Environ.* **2018**, *235*, 103-129; DOI 10.1016/j.apcatb.2018.04.044.

(21) Fernandez, D.; Robles, I.; Rodriguez-Valadez, F. J.; Godinez, L. A. Novel arrangement for an electro-Fenton reactor that does not require addition of iron, acid and a final neutralization stage. Towards the development of a cost-effective technology for the treatment of wastewater. *Chemosphere* **2018**, *199*, 251-255; DOI 10.1016/j.chemosphere.2018.02.036.

(22) Rostamizadeh, M.; Jafarizad, A.; Gharibian, S. High efficient decolorization of Reactive Red 120 azo dye over reusable Fe-ZSM-5 nanocatalyst in electro-Fenton reaction. *Sep. Purif. Technol.* **2018**, *192*, 340-347; DOI 10.1016/j.seppur.2017.10.041.

(23) Özcan, A.; Özcan, A. A.; Demirci, Y.; Şener, E. Preparation of Fe_2O_3 modified kaolin and application in heterogeneous electro-catalytic oxidation of enoxacin. *Appl. Catal. B: Environ.* **2017**, *200*, 361-371; DOI 10.1016/j.apcatb.2016.07.018.

(24) Ganiyu, S. O.; Le, T. X. H.; Bechelany, M.; Oturan, N.; Papirio, S.; Esposito, G.; van Hullebusch, E.; Cretin, M.; Oturan, M. A. Electrochemical mineralization of sulfamethoxazole over wide pH range using $Fe^{II}Fe^{III}$ LDH modified carbon felt cathode: Degradation pathway, toxicity and reusability of the modified cathode. *Chem. Eng. J.* **2018**, *350*, 844-855; DOI 10.1016/j.cej.2018.04.141.

(25) Expósito, E.; Sánchez-Sánchez, C. M.; Montiel, V. Mineral Iron oxides as iron source in electro-Fenton and photoelectro-Fenton mineralization processes. *J. Electrochem. Soc.* **2007**, *154*, E116−E122; DOI 10.1149/1.2744134.

(26) Ltaïef, A. H.; Sabatino, S.; Proietto, F.; Ammar, S.; Gadri, A.; Galia, A.; Scialdone, O. Electrochemical treatment of aqueous solutions of organic pollutants by

580 electro-Fenton with natural heterogeneous catalysts under pressure using Ti/IrO_2-Ta_2O_5
581 or BDD anodes. *Chemosphere* **2018**, *202*, 111-118; DOI
582 10.1016/j.chemosphere.2018.03.061.
583 (27) Mejide, J.; Pazos, M.; Sanromán, M. A. Heterogeneous electro-Fenton
584 catalyst for 1-butylpyridinium chloride degradation. *Environ. Sci. Pollut. Res.* **2019**, *26*,
585 3145-3156; DOI 10.1007/s11356-017-0403-6.
586 (28) Zhang, Y.; Tran, H. P.; Hussain, I.; Zhong, Y.; Huang. S. Degradation of *p*-
587 chloroaniline by pyrite in aqueous solutions. *Chem. Eng. J.* **2015**, *279*, 396-401; DOI
588 10.1016/j.cej.2015.03.016.
589 (29) Zhang, P.; Huang, W.; Ji, Z.; Zhou, C.; Yuan, S. Mechanisms of hydroxyl
590 radicals production from pyrite oxidation by hydrogen peroxide: surface versus aqueous
591 reactions. *Geochim. Cosmochim. Acta* **2018**, *238*, 394-410; DOI
592 10.1016/j.gca.2018.07.018.
593 (30) Labiadh, L.; Oturan, M. A.; Panizza, M.; Hamadi, N. B.; Ammar, S.
594 Complete removal of AHPS synthetic dye from water using new electro-fenton oxidation
595 catalyzed by natural pyrite as heterogeneous catalyst. *J. Hazard. Mater.* **2015**, *297*, 34-
596 41; DOI 10.1016/j.jhazmat.2015.04.062.
597 (31) Barhoumi, N.; Labiadh, L.; Oturan, M. A.; Oturan, N.; Gadri, A.; Ammar, S.;
598 Brillas, E. Electrochemical mineralization of the antibiotic levofloxacin by electro-
599 Fenton-pyrite process. *Chemosphere* **2015**, *141*, 250-257; DOI
600 10.1016/j.chemosphere.2015.08.003.
601 (32) Barhoumi, N.; Oturan, N.; Olvera-Vargas, H.; Brillas, E.; Gadri, A.; Ammar,
602 S.; Oturan, M. A. Pyrite as a sustainable catalyst in electro-Fenton process for improving
603 oxidation of sulfamethazine. Kinetics, mechanism and toxicity assessment. *Water Res.*
604 **2016**, *94*, 52-61; DOI 10.1016/j.watres.2016.02.042.

(33) Liu, W.; Wang, Y.; Ai, Z.; Zhang, L. Hydrothermal synthesis of FeS_2 as a high-efficiency Fenton reagent to degrade alachlor via superoxide-mediated Fe(II)/Fe(III) cycle. *ACS Appl. Mater. Interf.* **2015**, *7*, 28534-28544; DOI 10.1021/acsami.5b09919.

(34) Choe, Y. J.; Byun, J. Y.; Kim, S. H.; Kim, J. Fe_3S_4/Fe_7S_8-promoted degradation of phenol via heterogeneous, catalytic H_2O_2 scission mediated by S-modified surface Fe^{2+} species. *Appl. Catal. B: Environ.* **2018**, *233*, 272-280; DOI 10.1016/j.apcatb.2018.03.110.

(35) Liu, W.; Xu, L.; Li, X.; Shen, C.; Rashid, S.; Wen, Y.; Liu, W.; Wu, X. High-dispersive FeS_2 on graphene oxide for effective degradation of 4-chlorophenol. *RSC Adv.* **2015**, *5*, 2449-2456; DOI 10.1039/c4ra11354c.

(36) Dias, E. M.; Petit, C. Towards the use of metal–organic frameworks for water reuse: a review of the recent advances in the field of organic pollutants removal and degradation and the next steps in the field. *J. Mater. Chem. A* **2015**, *3*, 22484-22506; DOI 10.1039/c5ta05440k.

(37) Li, X.; Wang, B.; Cao, Y.; Zhao, S.; Wang, H.; Feng, X.; Zhou, J.; Ma, X. Water contaminant elimination based on metal–organic frameworks and perspective on their industrial applications. *ACS Sustain. Chem. Eng.* **2019**, *7*, 4548-4563; DOI 10.1021/acssuschemeng.8b05751.

(38) Liu, X.; Zhou, Y.; Zhang, J.; Tang, L.; Luo, L.; Zeng, G. Iron containing metal-organic frameworks: structure, synthesis, and applications in environmental remediation. *ACS Appl. Mater. Interf.* **2017**, *9*, 20255-20275; DOI 10.1021/acsami.7b02563.

(39) Cheng, M.; Lai, C.; Liu, Y.; Zeng, G.; Huang, D.; Zhang, C.; Qin, L.; Hu, L.; Zhou, C.; Xiong, W. Metal-organic frameworks for highly efficient heterogeneous

Fenton-like catalysis. *Coord. Chem. Rev.* **2018**, *368*, 80-92; DOI 10.1016/j.ccr.2018.04.012.

(40) Sharma, V. K.; Feng, M. Water depollution using metal-organic frameworks-catalyzed advanced oxidation processes: a review. *J. Hazard. Mater.* **2019**, *372*, 3-16; DOI 10.1016/j.jhazmat.2017.09.043.

(41) Gao, C.; Chen, S.; Quan, X.; Yu, H.; Zhang, Y. Enhanced Fenton-like catalysis by iron-based metal organic frameworks for degradation of organic pollutants. *J. Catal.* **2017**, *356*, 125-132; DOI 10.1016/j.jcat.2017.09.015.

(42) Tang, J; Wang, J. Metal organic framework with coordinatively unsaturated sites as efficient Fenton-like catalyst for enhanced degradation of sulfamethazine. *Environ. Sci. Technol.* **2018**, *52*, 5367-5377; DOI 10.1021/acs.est.8b00092.

(43) Chen, D.; Chen, S.; Jiang, Y.; Xie, S.; Quan, H.; Hua, L.; Luo, X.; Guo, L. Heterogeneous Fenton-like catalysis of Fe-MOF derived magnetic carbon nanocomposites for degradation of 4-nitrophenol. *RSC Adv.* **2017**, *7*, 49024-49030; DOI 10.1039/c7ra09234b.

(44) Tang, J; Wang, J. Fenton-like degradation of sulfamethoxazole using Fe-based magnetic nanoparticles embedded into mesoporous carbon hybrid as an efficient catalyst. *Chem. Eng. J.* **2018**, *351*, 1085-1094; DOI 10.1016/j.cej.2018.06.169.

(45) Zhao, H., Chen, Y.; Peng, Q.; Wang, Q.; Zhao, G. Catalytic activity of MOF(2Fe/Co)/carbon aerogel for improving H_2O_2 and $^{\bullet}OH$ generation in solar photo–electro–Fenton process. *Appl. Catal. B: Environ.* **2017**, *203*, 127-137; DOI 10.1016/j.apcatb.2016.09.074.

(46) Le, T. X. H.; Cowan, M. G.; Drobek, M.; Bechelany M.; Julbe, A.; Cretin, M. Fe-Nanoporous carbon derived from MIL-53(Fe): a heterogeneous catalyst for

mineralization of organic pollutants. *Nanomaterials* **2019**, *9*, 641; DOI 10.3390/nano9040641.

(47) Liu, K.; Yu, M.; Wang, H.; Wang, J.; Liu, W.; Hoffmann, M. R. Multiphase porous electrochemical catalysts derived from Iron-based metal−organic framework compounds. *Environ. Sci. Technol.* **2019**, *53*, 6474-6482; DOI 10.1021/acs.est.9b01143.

(48) Jennifer Ebele, A.; Abou-Elwafa Abdallah, M. Harrad, S. Pharmaceuticals and personal care products (PPCPs) in the freshwater aquatic environment. *Emerging Contam.* **2017**, *3*, 1-16; DOI 10.1016/j.emcon.2016.12.004.

(49) Bagnis, S.; Fitzsimons, M. F.; Snape, J.; Tappin, A.; Comber, S. Processes of distribution of pharmaceuticals in surface freshwaters: implications for risk assessment. *Environ. Chem. Lett.* **2018**, *16*, 1193-1216; DOI 10.1007/s10311-018-0742-7.

(50) Debiolles, F.; Malleret, L.; Tiliacos, C.; Wong-Wah-Chung, P.; Laffont-Schwob, I. Occurrence and ecotoxicological assessment of pharmaceuticals: is there a risk for the Mediterranean aquatic environment? *Sci. Total Environ.* **2018**, *639*, 1334-1348; DOI 10.1016/j.scitotenv.2018.04.351.

(51) Mezzelani, M.; Gorbi, S.; Regoli, F. Pharmaceuticals in the aquatic environments: Evidence of emerged threat and future challenges for marine organisms. *Marine Environ. Res.* **2018**, *140*, 41-60; DOI 10.1016/j.marenvres.2018.05.001.

(52) Sehonova, P.; Svobodova, Z.; Dolezelova, P.; Vosmerova, P.; Faggio, C. Effects of waterborne antidepressants on non-target animals living in the aquatic environment: a review. *Sci. Total Environ.* **2018**, *631-632*, 789-794; DOI 10.1016/j.scitotenv.2018.03.076.

(53) Vieno, N.; Hallgren, P.; Wallberg, P.; Phyhala, M.; Zandaryaa, S. Pharmaceuticals in the aquatic environment of the Baltic Sea region: a status report. *UNESCO Publishing* **2017**, 1-119.

(54) Salazar, C.; Ridruejo, C.; Brillas, E.; Yáñez, J.; Mansilla, H. D.; Sirés, I. Abatement of the fluorinated antidepressant fluoxetine (Prozac) and its reaction by-products by electrochemical advanced methods. *Appl. Catal. B: Environ.* **2017**, *203*, 189-198; DOI 10.1016/j.apcatb.2016.10.026.

(55) Pham, D. T.; Baboo, J. P.; Song, J.; Kim, S.; Jo, J.; Mathew, V.; Alfaruqi, M. H.; Sambandam, B.; Kim, J. Facile synthesis of pyrite (FeS_2/C) nanoparticles as an electrode material for non-aqueous hybrid electrochemical capacitors. *Nanoscale* **2018**, *10*, 5938-5949; DOI 10.1039/C7NR06352K.

(56) Chen, W.; Westerhoff, P.; Leenheer, J. A.; Booksh, K. Fluorescence excitation−emission matrix regional integration to quantify spectra for dissolved organic matter. *Environ. Sci. Technol.* **2003**, *37*, 5701-5710; DOI 10.1021/es034354c.

(57) Vera, M.; Martín-Alonso, J.; Mesa, J.; Granados, M.; Beltran, J. L.; Casas, S.; Gibert, O.; Cortina, J. L. Monitoring UF membrane performance treating surface-groundwater blends: Limitations of FEEM-PARAFAC on the assessment of the organic matter role. *Chem. Eng. J.* **2017**, *317*, 961-971; DOI 10.1016/j.cej.2017.02.081.

(58) Lu, Z.; Wang, N.; Zhang, Y.; Xue, P.; Guo, M.; Tang, B.; Xu, X.; Wang, W.; Bai, Z.; Dou, S. Metal−organic framework-derived sea-cucumber-like FeS_2@C nanorods with outstanding pseudocapacitive Na-ion storage properties. *ACS Appl. Energy Mater.* **2018**, *1*, 6234-6241; DOI 10.1021/acsaem.8b01239.

(59) Lu, Z.; Wang, N.; Zhang, Y.; Xue, P.; Guo, M.; Tang, B.; Bai, Z.; Dou, S. Pyrite FeS_2@C nanorods as smart cathode for sodium ion battery with ultra-long lifespan and notable rate performance from tunable pseudocapacitance. *Electrochim. Acta* **2018**, *260*, 755-761; DOI 10.1016/j.electacta.2017.12.031.

(60) Chen, J.; Zhou, X.; Mei, C.; Xu, J.; Zhou, S.; Wong, C. P. Pyrite FeS_2 nanobelts as high-performance anode material for aqueous pseudocapacitor. *Electrochim. Acta* **2016**, *222*, 172-176; DOI 10.1016/j.electacta.2016.10.181.

(61) Liang, P.; Zhang, C.; Duan, X.; Sun, H.; Liu, S.; Tade, M. O.; Wang, S. An insight into metal organic framework derived N-doped graphene for the oxidative degradation of persistent contaminants: formation mechanism and generation of singlet oxygen from peroxymonosulfate. *Environ. Sci. Nano* **2017**, *4*, 315-324; DOI 10.1039/c6en00633g.

(62) Zhuang, Y.; Yuan, S.; Liu, J.; Zhang, Y.; Du, H.; Wu, C.; Zhao, P.; Chen, H.; Pei, Y. Synergistic effect and mechanism of mass transfer and catalytic oxidation of octane degradation in yolk-shell Fe_3O_4@C/Fenton system. *Chem. Eng. J.* **2020**, *379*, 122262; DOI 10.1016/j.cej.2019.122262.

(63) Bedner, M.; MacCrehan, W. A. Reactions of the amine-containing drugs fluoxetine and metoprolol during chlorination and dechlorination processes used in wastewater treatment. *Chemosphere* **2006**, *65*, 2130-2137; DOI 10.1016/j.chemosphere.2006.06.016.

(64) Coria, G.; Sirés, I.; Brillas, E.; Nava, J. L. Influence of the anode material on the degradation of naproxen by Fenton-based electrochemical processes. *Chem. Eng. J.* **2016**, *304*, 817-825; DOI 10.1016/j.cej.2016.07.012.

(65) Martín-García, L.; Bernal-Villamil, I.; Oujja, M.; Carrasco, E.; Gargallo-Caballero, R.; Castillejo, M.; Marco, J. F.; Gallego, S.; de la Figuera, J. Unconventional properties of nanometric FeO(111) films on Ru(0001): stoichiometry and surface structure. *J. Mater. Chem. C* **2016**, *4*, 1850-1859; DOI 10.1039/c5tc03871e.

(66) Unceta, N.; Barrondo, S.; Ruiz de Azúa, I.; Gómez-Caballero, A.; Goicolea, M. A.; Sallés, J.; Barrio, R. J. Determination of fluoxetine, norfluoxetine and their

726 enantiomers in rat plasma and brain samples by liquid chromatography with fluorescence
727 detection. *J. Chromatogr. B* **2007**, *852*, 519-528; DOI 10.1016/j.jchromb.2007.02.008.
728

Figure captions

Figure 1. (a) SEM image at 33,000×, (b) XRD pattern, (c,d,e) TEM analysis and (f) site of interest along with EDS elemental mapping for the as-synthesized catalyst. In (b), the symbols account for the peaks related to (▼) FeS_2 pyrite (JCPDS 65-1211), and (◆) Fe_2O_3 (JCPDS 89-0597) references.

Figure 2. XPS spectrum of different elements present in the FeS_2 nanocatalyst: (a) Fe 2p, (b) S 2p, and (c) N 1s.

Figure 3. (a) Normalized fluoxetine concentration decay during the treatment of solutions containing 0.049 mM drug (10 mg C L^{-1}) spiked into 150 mL of urban wastewater by (×) EO-H_2O_2 at initial pH 3.0, (□) conventional EF with 5 mg L^{-1} Fe^{2+} at initial pH 3.0, and heterogeneous EF (▲) with 0.5 g L^{-1} natural pyrite at initial pH 6.0, and (◆) with 0.5 g L^{-1} FeS_2/C nanocatalyst at initial pH 6.0. Comparison with (▽) EO-H_2O_2 in 0.05 M Na_2SO_4 is shown. All trials were carried out with an IrO_2/air-diffusion cell at 50 mA and 30 °C. (b) Final pH (filled bar) and iron concentration (dashed bar) after 60 min of the heterogeneous EF trials.

Figure 4. Time course of normalized fluoxetine concentration during the heterogeneous EF treatment of 150 mL of 0.049 mM drug (10 mg C L^{-1}) solutions, prepared with urban wastewater, using an IrO_2/air-diffusion cell (except in plot d) with the FeS_2/C nanocatalyst at 30 ºC. (a) Effect of pH, with 0.5 g L^{-1} nanocatalyst at 50 mA. Initial pH: (●) 8.0, (■) 7.0, (◆) 6.0, (▲) 5.0, and (▼) 4.0. (b) Effect of nanocatalyst dose, at pH 6.0 and 50 mA. Content: (○) 0.1, (□) 0.2, (△) 0.3, (▽) 0.4, and (◆) 0.5 g L^{-1} FeS_2/C. (c) Effect of applied current, at pH 6.0 with 0.5 g L^{-1} nanocatalyst. Current: (◣) 15, (◢) 30, and (◆) 50 mA. (d) Effect of anode, at pH 6.0 with 0.5 g L^{-1} nanocatalyst at 50 mA. Anode: (◆) IrO_2-based, (▷) RuO_2based, and (◁) BDD.

Figure 5. (a) FEEM spectra of: (1) urban wastewater at natural pH 6.0 after stripping, (2) same matrix with fluoxetine spiked at 0.098 mM, and samples withdrawn after (3) 1 h, (4) 2 h, (5) 3 h, (6) 4 h, and (7) 5 h of heterogeneous EF treatment of 150 mL of 0.098 mM drug solutions in urban wastewater with 0.4 g L^{-1} FeS_2/C nanocatalyst at pH 6.0 using a BDD/air-diffusion cell at 100 mA and 30 ºC. (b) Distribution of PARAFAC-derived components C1-C5 in samples 1-7 of plot (a).

Figure 6. Proposed mechanism for FeS_2/C-catalyzed heterogeneous EF treatment at mild pH.

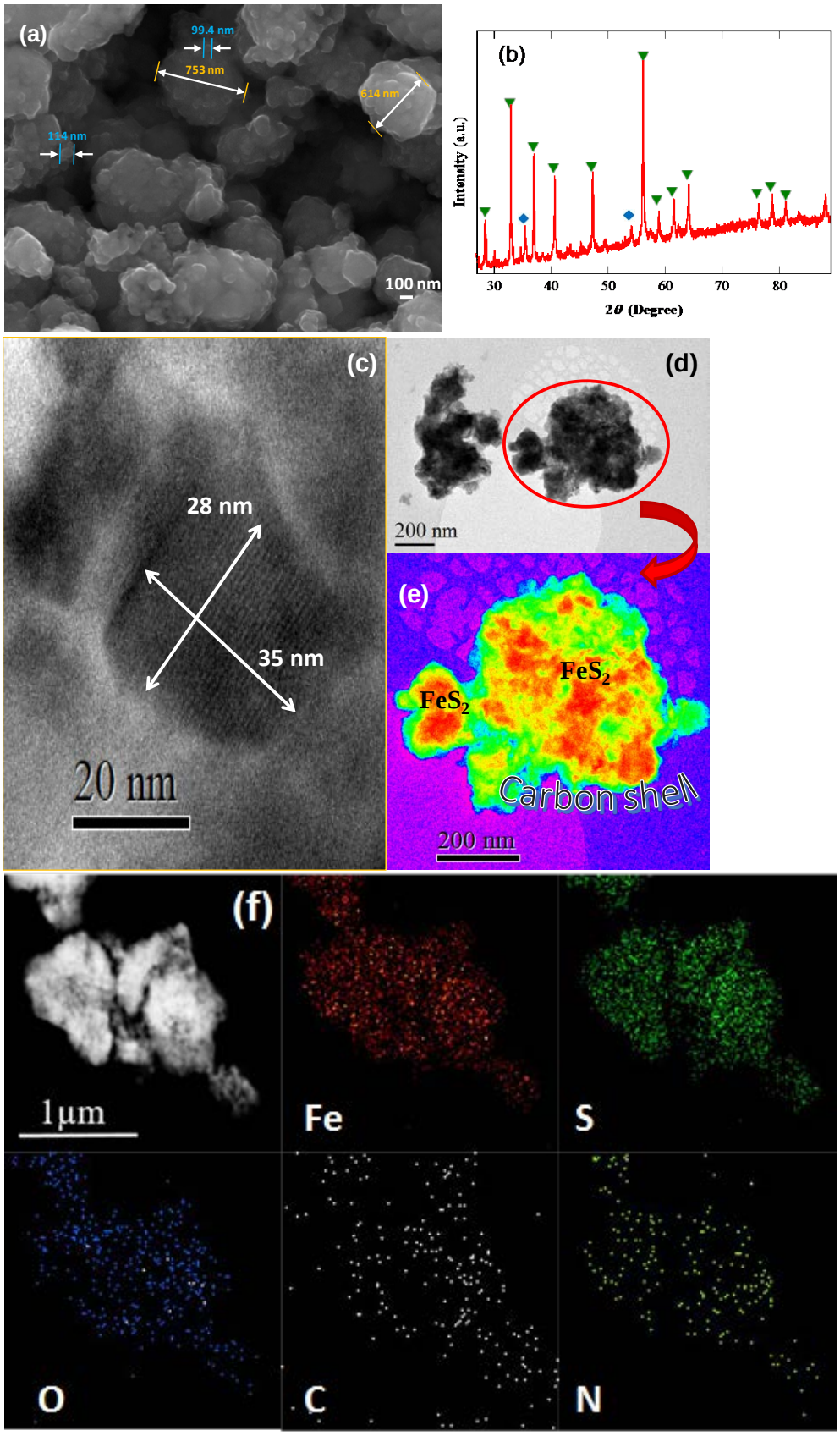
(a)
99.4 nm
753 nm
614 nm
114 nm
100 nm
(b)
Intensity (a.u.)
30
40
50
60
70
80
2θ (Degree)
(c)
28 nm
35 nm
20 nm
(d)
200 nm
(e)
FeS2
FeS2
Carbon shell
200 nm
(f)
1μm
Fe
S
O
C
N

Figure 1

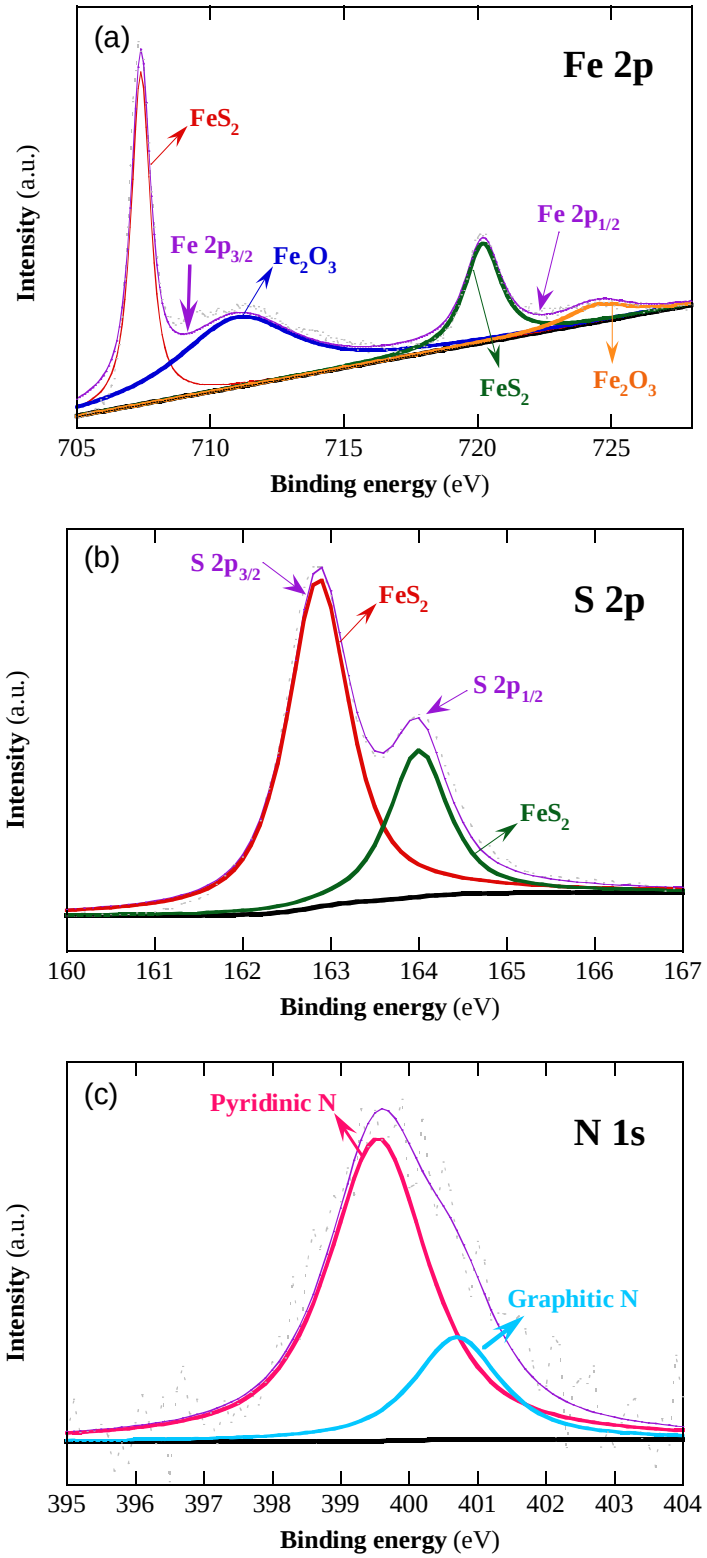
(a)
Fe 2p
FeS2
Fe 2p3/2
Fe2O3
Fe 2p1/2
FeS2
Fe2O3
Intensity (a.u.)
705
710
715
720
725
Binding energy (eV)
(b)
S 2p3/2
FeS2
S 2p
S 2p1/2
FeS2
Intensity (a.u.)
160
161
162
163
164
165
166
167
Binding energy (eV)
(c)
Pyridinic N
N 1s
Graphitic N
Intensity (a.u.)
395
396
397
398
399
400
401
402
403
404
Binding energy (eV)

Figure 2

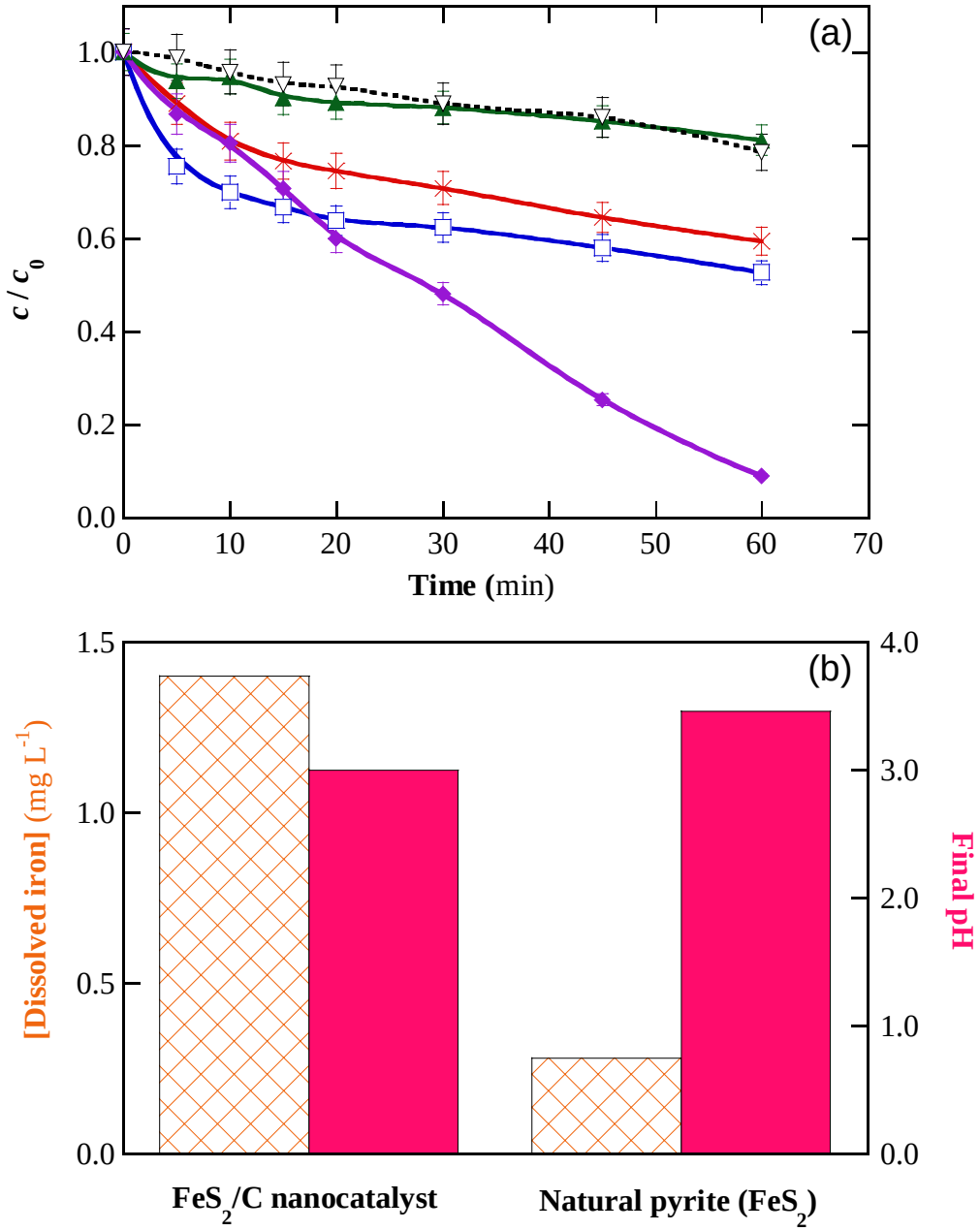
(a)
1.0
0.8
0.6
0.4
0.2
0.0
c / c0
0
10
20
30
40
50
60
70
Time (min)
(b)
1.5
1.0
0.5
0.0
[Dissolved iron] (mg L-1)
4.0
3.0
2.0
1.0
0.0
Final pH
FeS2/C nanocatalyst
Natural pyrite (FeS2)

Figure 3

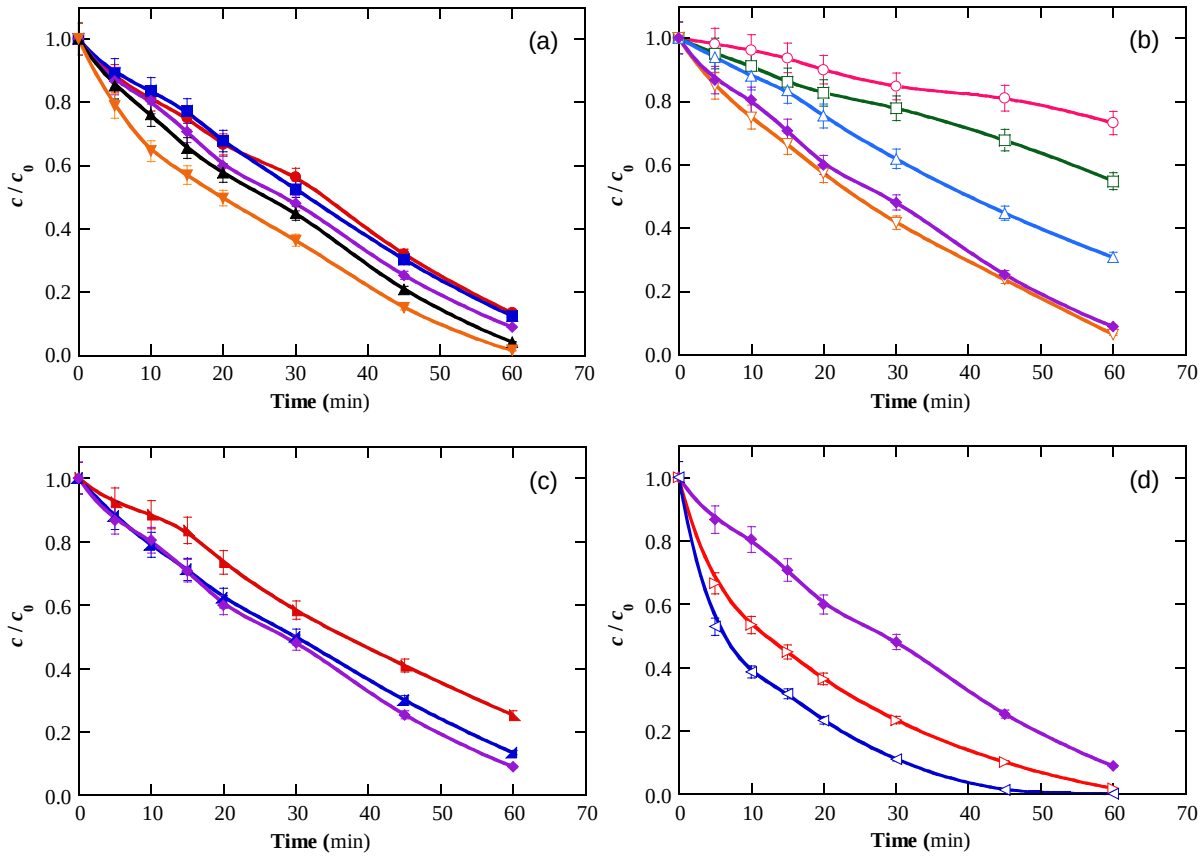

Figure 4

(a)

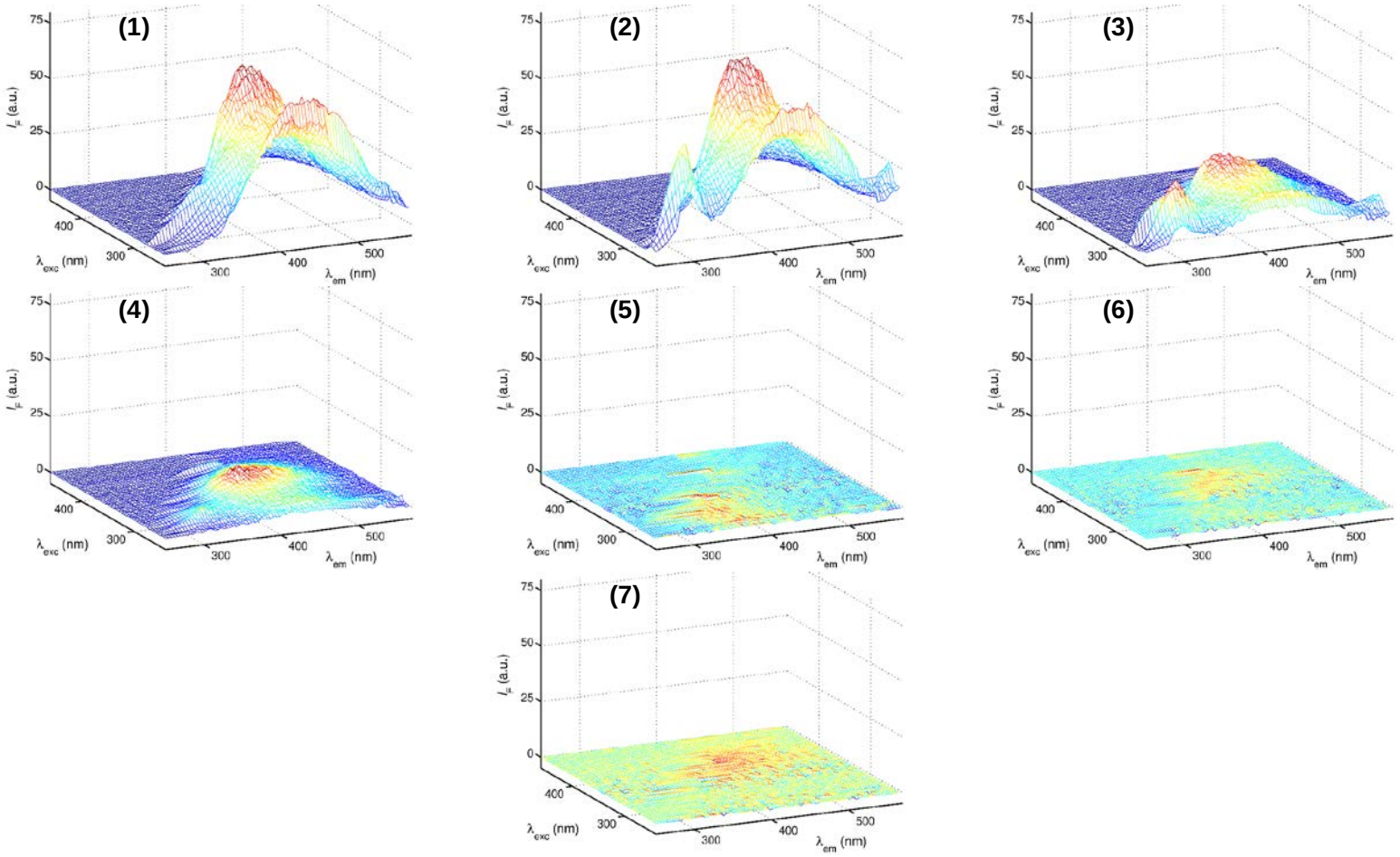
(1)
(2)
(3)
(4)
(5)
(6)
(7)
I_F (a.u.)
λ_{exc} (nm)
λ_{em} (nm)

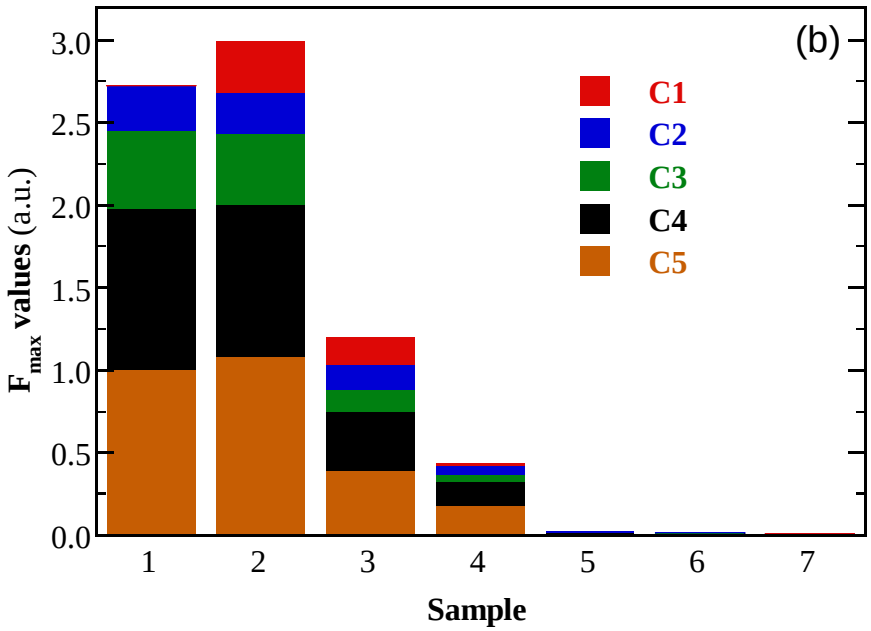
(b)
C1
C2
C3
C4
C5
F_{max} values (a.u.)
Sample

Figure 5

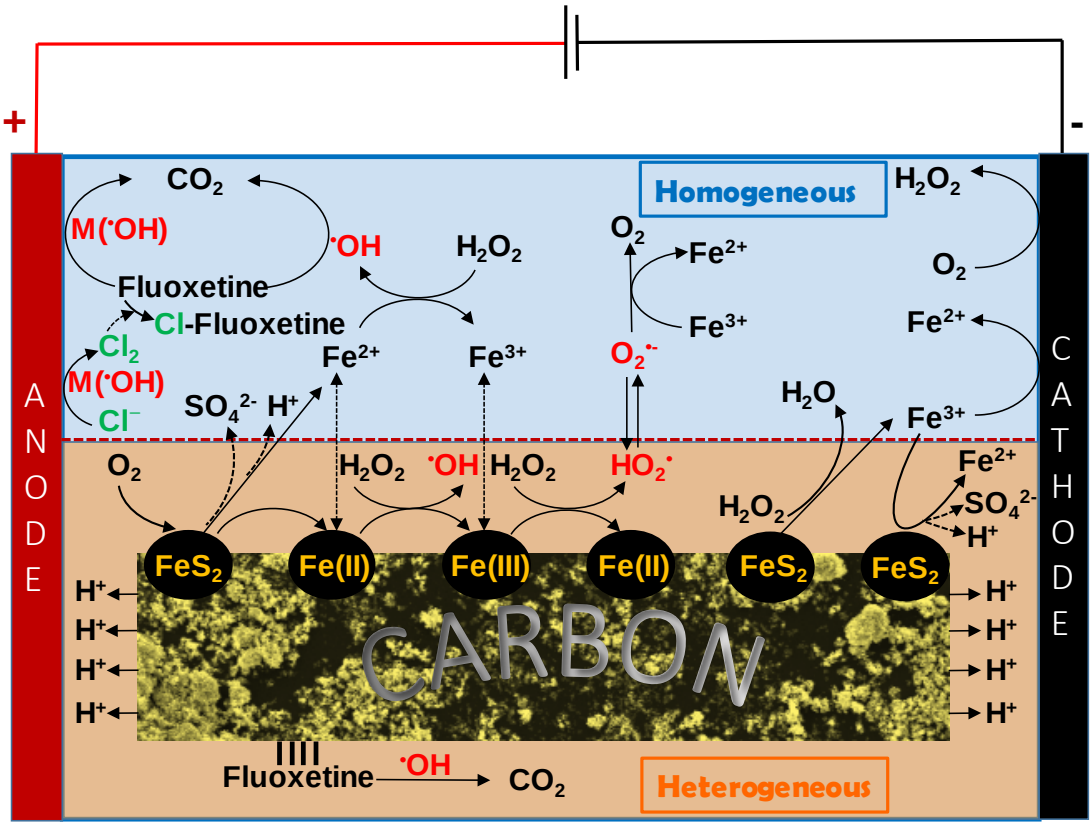
+
-
ANODE
CATHODE
Homogeneous
Heterogeneous
CARBON
CO2
M(·OH)
Fluoxetine
Cl-Fluoxetine
Cl2
Cl−
·OH
H2O2
Fe2+
Fe3+
O2
O2·-
HO2·
SO4 2- H+
H2O
FeS2
Fe(II)
Fe(III)
Fe(II)
FeS2
FeS2
H+
Fluoxetine
·OH
CO2

Figure 6